The 8th European Congress on Computational Methods in Applied Sciences and Engineering
ECCOMAS Congress 2022
5–9 June 2022, Oslo, Norway

MIXED FINITE ELEMENT FORMULATIONS AND ENERGY-MOMENTUM TIME INTEGRATORS FOR THERMO-VISCOELASTIC GRADIENT-BASED FIBER-REINFORCED CONTINUA

JULIAN DIETZSCH[1], MICHAEL GROSS[2] AND INIYAN KALAIMANI[3]

[1] Technische Universität Chemnitz
Professorship of applied mechanics and dynamics
Reichenhainer Straße 70, D-09126 Chemnitz
e-mail: julian.dietzsch@mb.tu-chemnitz.de,
[2] michael.gross@mb.tu-chemnitz.de,
[3] iniyan.kalaimani@mb.tu-chemnitz.de

Key words: Energy-momentum schemes, fiber-bending stiffness, locking behavior, mixed finite elements, mixed variational principle, gradient elasticity.

Abstract. Nowadays, fibre-reinforced materials and their accurate dynamic simulation play a significant role in the construction of lightweight structures. On the one hand, we are dealing with locking of the matrix material as well as the fibres, thermal expansion, the directed heat conduction through the fibres and viscoelastic behaviour in such materials. The material reinforcement is performed by fiber rovings with a separate bending stiffness, which can be modelled by second order gradients. On the other hand, we also want to perform accurate long-term simulations. In this presentation, we focus on numerically stable dynamic long-time simulations with locking free meshes, and thus use higher-order accurate energy-momentum schemes emanating from mixed finite element methods. We adapt the variational-based space-time finite element method in Reference [1] to the material formulation, and additionally include independent fields to obtain well-known mixed finite elements [2, 3].

1 INTRODUCTION

An anisotropic material with a thermo-viscoelastic matrix and a thermo-viscoelastic fiber roving with n_{F} fiber orientations $\boldsymbol{a}_0$ is considered moving in the Euclidean space $\mathbb{R}^{n_{\mathrm{dim}}}$ with the constant ambient temperature Θ_∞. We formulate a strain energy function for this material as an additive split of matrix part Ψ_{M}, a fiber part regarding to the fiber roving stretch Ψ_{F} and a higher-order gradient part regarding to the bending for the fiber roving Ψ_{H} and is given by

$$\Psi(\boldsymbol{C},\boldsymbol{C}_{\mathrm{v}}^{\mathrm{M}},\Theta,\boldsymbol{C}_{\mathrm{v}}^{\mathrm{F}_i},\boldsymbol{a}_0^i) = \Psi_{\mathrm{M}}(\boldsymbol{C},\boldsymbol{C}_{\mathrm{v}}^{\mathrm{M}},\Theta) + \sum_{i=1}^{n_{\mathrm{F}}} \left[\Psi_{\mathrm{F}_i}(\boldsymbol{C},\boldsymbol{C}_{\mathrm{v}}^{\mathrm{F}_i},\Theta,\boldsymbol{a}_0^i) + \Psi_{\mathrm{H}_i}(\nabla\boldsymbol{C},\boldsymbol{C},\boldsymbol{a}_0^i)\right]. \tag{1}$$

The deformation gradient by the position $\boldsymbol{q}$ is defined by $\boldsymbol{F} = \nabla\boldsymbol{q}$, the right Cauchy-Green tensor is defined by $\boldsymbol{C} = \boldsymbol{F}^T\boldsymbol{F}$, the viscous right Cauchy-Green tensor with respect to the matrix is defined by $\boldsymbol{C}_{\mathrm{v}}^{\mathrm{M}}$, the viscous right Cauchy-Green tensor with respect to the fiber is defined by $\boldsymbol{C}_{\mathrm{v}}^{\mathrm{F}_i}$, the gradient of $\boldsymbol{C}$ is

defined by $\nabla \boldsymbol{C}$ and Θ is the absolute temperature. Their corresponding dependencies are given as

$$\begin{aligned}\Psi_{\mathrm{M}}(\boldsymbol{C},\mathrm{cof}[\boldsymbol{C}],J,\boldsymbol{C}_{\mathrm{v}}^{\mathrm{M}},\Theta) &= \Psi_{\mathrm{M}}^{\mathrm{iso}}(\boldsymbol{C},\mathrm{cof}[\boldsymbol{C}],J)+\Psi_{\mathrm{M}}^{\mathrm{vol}}(J)+\Psi_{\mathrm{M}}^{\mathrm{cap}}(\Theta)+\Psi_{\mathrm{M}}^{\mathrm{coup}}(\Theta,J)+\Psi_{\mathrm{M}}^{\mathrm{vis}}(\boldsymbol{C}(\boldsymbol{C}_{\mathrm{v}}^{\mathrm{M}})^{-1})\\ \Psi_{\mathrm{F}_i}(\boldsymbol{C},\mathrm{cof}[\boldsymbol{C}],J,\boldsymbol{C}_{\mathrm{v}}^{\mathrm{F_i}},\boldsymbol{a}_0^i,\Theta) &= \Psi_{\mathrm{F}_i}^{\mathrm{ela}}(\boldsymbol{C},\mathrm{cof}[\boldsymbol{C}],\boldsymbol{a}_0^i)+\Psi_{\mathrm{F}_i}^{\mathrm{cap}}(\Theta)+\Psi_{\mathrm{F}_i}^{\mathrm{coup}}(\Theta,\boldsymbol{C})+\Psi_{\mathrm{F}_i}^{\mathrm{vis}}(\boldsymbol{C}(\boldsymbol{C}_{\mathrm{v}}^{\mathrm{F_i}})^{-1}),\end{aligned}$$

with the volume dilatation $J(\boldsymbol{C})=\det[\boldsymbol{F}]=\sqrt{\det[\boldsymbol{C}]}$. The free energy function of matrix Ψ_{M} and fiber Ψ_{F} are further split into their corresponding elastic parts ($\Psi_{\mathrm{M}}^{\mathrm{iso}},\Psi_{\mathrm{M}}^{\mathrm{vol}},\Psi_{\mathrm{F}_i}^{\mathrm{ela}}$), heat capacity part ($\Psi_{\mathrm{M}}^{\mathrm{cap}},\Psi_{\mathrm{F}_i}^{\mathrm{cap}}$), thermo-mechanical coupling part ($\Psi_{\mathrm{M}}^{\mathrm{coup}},\Psi_{\mathrm{F}}^{\mathrm{coup}}$) and viscoelastic free energy function ($\Psi_{\mathrm{M}}^{vis},\Psi_{\mathrm{F}}^{vis}$). The functions of the thermo-mechanical coupling are given by

$$\Psi_{\mathrm{M}}^{\mathrm{coup}}=-2n_{\mathrm{dim}}\beta_{\mathrm{M}}(\Theta-\Theta_\infty)J\frac{\partial\Psi_{\mathrm{M}}^{\mathrm{vol}}(J)}{\partial J}\quad \Psi_{\mathrm{F}_i}^{\mathrm{coup}}=-2\beta_{\mathrm{F}}(\Theta-\Theta_\infty)\sqrt{I_4^i}\frac{\partial\Psi_{\mathrm{F}}^{\mathrm{ela}}(I_4^i,\dots)}{\partial I_4^i} \tag{2}$$

where β_{M} and β_{F_i} is the coefficient of linear thermal expansion, $\boldsymbol{M}^i=\boldsymbol{a}_0^i\otimes\boldsymbol{a}_0^i$ is the structural tensor and the fourth invariant $I_4^i=\mathrm{tr}[\boldsymbol{C}\boldsymbol{M}^i]$. In Reference [4] we compare two different variants for the higher-order gradient part Ψ_{H_i}. One with respect to the gradient of the deformation gradient $\boldsymbol{F}$ (see Reference [5]) and the second with respect to the gradient of the right Cauchy-Green tensor $\boldsymbol{C}$ (see Reference [6]). We are able to show that formulation in $\boldsymbol{C}$ also works. This has several advantages, such as a simpler weak form, the possibility to formulate the energy-momentum scheme directly in $\nabla\boldsymbol{C}$, the possibility to use multiple fibers, and as result a less expensive numerical calculation. The sixth invariant of this formulation is given by

$$I_6^C(\nabla\boldsymbol{C})=(\boldsymbol{a}_0\cdot\nabla\boldsymbol{C}\cdot\boldsymbol{a}_0)\cdot(\boldsymbol{a}_0\cdot\nabla\boldsymbol{C}\cdot\boldsymbol{a}_0) \tag{3}$$

If we now set

$$\boldsymbol{\Lambda}(\nabla\boldsymbol{C})=\boldsymbol{a}_0\cdot\nabla\boldsymbol{C} \tag{4}$$

we get the same expressions for the invariants as for $\boldsymbol{F}$ (see Reference [5]), given by

$$I_6(\nabla\boldsymbol{C})=\boldsymbol{\kappa}_0\cdot\boldsymbol{\kappa}_0\qquad I_7(\boldsymbol{C},\nabla\boldsymbol{C})=\boldsymbol{\kappa}_0\cdot\boldsymbol{C}\cdot\boldsymbol{\kappa}_0 \tag{5}$$

with $\boldsymbol{\kappa}_0=\boldsymbol{\Lambda}\cdot\boldsymbol{a}_0$ and the final dependencies read

$$\Psi_{\mathrm{H}_i}(\nabla\boldsymbol{C},\boldsymbol{C},\boldsymbol{a}_0^i)=f(I_6(\nabla\boldsymbol{C}),I_7(\nabla\boldsymbol{C},\boldsymbol{C})) \tag{6}$$

2 FINITE ELEMENT FORMULATION

We derive the weak forms based on the mixed principle of virtual power as in Reference [1, 7]. Here, we need the complete internal energy, which consists of the assumed temperature field $\tilde{\Theta}$, the entropy density field η as the corresponding Lagrange multiplier, an independent mixed field $\tilde{\boldsymbol{F}}$ with the corresponding Lagrange multiplier $\tilde{\boldsymbol{P}}$, an independent mixed field $\tilde{\boldsymbol{C}}$ and the corresponding Lagrange multiplier $\tilde{\boldsymbol{S}}$. In addition, we introduce the viscous right Cauchy-Green tensor for the matrix $\tilde{\boldsymbol{C}}_{\mathrm{v}}^{\mathrm{M}}$ as well as the fiber $\tilde{\boldsymbol{C}}_{\mathrm{v}}^{\mathrm{F}_i}$ as an independent mixed field. The internal energy functional reads

$$\begin{aligned}\Pi^{\mathrm{int}}=&\int_{\mathcal{B}_0}\Psi_{\mathrm{M}}(\tilde{\boldsymbol{C}},\tilde{\boldsymbol{H}},\tilde{J},\tilde{\boldsymbol{C}}_{\mathrm{v}}^{\mathrm{M}},\Theta)\mathrm{d}V+\sum_{i=1}^{n_{\mathrm{F}}}\int_{\mathcal{B}_0}\Psi_{\mathrm{F}_i}(\tilde{\boldsymbol{C}}_A,\tilde{\boldsymbol{H}}_A,\tilde{J}_A,\tilde{\boldsymbol{C}}_{\mathrm{v}}^{\mathrm{F_i}},\boldsymbol{a}_0^i,\Theta)\mathrm{d}V+\sum_{i=1}^{n_{\mathrm{F}}}\int_{\mathcal{B}_0}\Psi_{\mathrm{H}_i}(\tilde{\boldsymbol{\Gamma}},\tilde{\boldsymbol{C}}_A,\boldsymbol{a}_0^i)\mathrm{d}V\\ &\int_{\mathcal{B}_0}\tilde{\boldsymbol{P}}:(\boldsymbol{F}(\boldsymbol{q})-\tilde{\boldsymbol{F}})\mathrm{d}V+\frac{1}{2}\int_{\mathcal{B}_0}\tilde{\boldsymbol{S}}:(\tilde{\boldsymbol{F}}^T\tilde{\boldsymbol{F}}-\tilde{\boldsymbol{C}})\mathrm{d}V+\int_{\mathcal{B}_0}\eta\,(\Theta-\tilde{\Theta})+\Pi_{\mathrm{M}}^{\mathrm{int}}+\Pi_{\mathrm{H}}^{\mathrm{int}}\end{aligned} \tag{7}$$

To avoid locking effects, we introduce independent variable fields $\tilde{J}$ for volume dilatation as in Reference [8], an independent variable $\tilde{\boldsymbol{H}}$ for the cofactor of $\tilde{\boldsymbol{C}}$ as in Reference [9], an independent field $\tilde{\boldsymbol{C}}_A$ for the anisotropic part Ψ_{F} as in Reference [2]. Additionally we add the additional fields $\tilde{\boldsymbol{H}}_A$ and $\tilde{J}_A$ as shown in Reference [7]. Here, the hydrostatic pressure p and the stress tensor $\boldsymbol{S}_A$ are described as Lagrange multipliers corresponding to volume dilatation and to anisotropic part respectively.

$$\begin{aligned}\Pi_{\mathrm{M}}^{\mathrm{int}} = &\int_{\mathcal{B}_0} p\,(J(\tilde{\boldsymbol{C}}) - \tilde{J})\mathrm{d}V + \int_{\mathcal{B}_0} \tilde{\boldsymbol{B}} : (\mathrm{cof}[\tilde{\boldsymbol{C}}] - \tilde{\boldsymbol{H}})\mathrm{d}V + \frac{1}{2}\int_{\mathcal{B}_0} \boldsymbol{S}_A : (\tilde{\boldsymbol{C}} - \tilde{\boldsymbol{C}}_A)\mathrm{d}V \\ &+ \int_{\mathcal{B}_0} \tilde{\boldsymbol{B}}_A : (\mathrm{cof}[\tilde{\boldsymbol{C}}] - \tilde{\boldsymbol{H}}_A)\mathrm{d}V + \int_{\mathcal{B}_0} p_A\,(J(\tilde{\boldsymbol{C}}) - \tilde{J}_A)\mathrm{d}V \end{aligned} \tag{8}$$

The advantage of the definition of independent field $\tilde{\boldsymbol{\Gamma}}$ for $\nabla\tilde{\boldsymbol{C}}$ is to eliminate the construction of double gradient of the spatial shape functions later in the discrete setting.

$$\Pi_{\mathrm{H}}^{\mathrm{int}} = \int_{\mathcal{B}_0} \boldsymbol{B}_G \odot_3 (\nabla(\tilde{\boldsymbol{C}}) - \tilde{\boldsymbol{\Gamma}})\mathrm{d}V\mathrm{d}V \tag{9}$$

For the mixed principle of virtual power, we also need the kinetic power, given by

$$\dot{T} = \int_{\mathcal{B}_0} (\rho_0 \boldsymbol{v} - \boldsymbol{p}) \cdot \dot{\boldsymbol{v}}\mathrm{d}V + \int_{\mathcal{B}_0} \dot{\boldsymbol{p}} \cdot (\dot{\boldsymbol{q}} - \boldsymbol{v})\mathrm{d}V + \int_{\mathcal{B}_0} \boldsymbol{p} \cdot \ddot{\boldsymbol{q}}\mathrm{d}V \tag{10}$$

with the velocity $\boldsymbol{v}$, the linear momentum $\boldsymbol{p}$ and the mass density ρ_0. We define the external power as,

$$\begin{aligned}\dot{\Pi}^{\mathrm{ext}} = &-\int_{\partial\mathcal{B}_0} \boldsymbol{t} \cdot \dot{\boldsymbol{q}}\mathrm{d}V - \int_{\mathcal{B}_0} \rho_0 \boldsymbol{g} \cdot \dot{\boldsymbol{q}}\mathrm{d}V - \int_{\partial\mathcal{B}_0} \boldsymbol{\lambda}_q \cdot (\dot{\boldsymbol{q}} - \dot{\boldsymbol{q}}^{\mathrm{ref}})\mathrm{d}A - \int_{\partial\mathcal{B}_0} \boldsymbol{\lambda}_\Theta \cdot (\dot{\Theta} - \dot{\Theta}^{\mathrm{ref}})\mathrm{d}A + \frac{1}{2}\int_{\mathcal{B}_0} \overline{\tilde{\boldsymbol{S}}} : \dot{\tilde{\boldsymbol{C}}}\mathrm{d}V \\ &+ \int_{\mathcal{B}_0} \nabla\left(\frac{\tilde{\Theta}}{\Theta}\right) \cdot \boldsymbol{Q}\mathrm{d}V + \int_{\mathcal{B}_0} \frac{\tilde{\Theta}}{\Theta} D^{\mathrm{int}}(\tilde{\boldsymbol{C}}_{\mathrm{v}}^{\mathrm{M}})\mathrm{d}V + \frac{1}{2}\int_{\mathcal{B}_0} \dot{\tilde{\boldsymbol{C}}}_{\mathrm{v}}^{\mathrm{M}} : \mathbb{V}(\tilde{\boldsymbol{C}}_{\mathrm{v}}^{\mathrm{M}}) : \dot{\tilde{\boldsymbol{C}}}_{\mathrm{v}}^{\mathrm{M}}\mathrm{d}V + \sum_{i=1}^{n_{\mathrm{F}}} \int_{\mathcal{B}_0} \frac{\tilde{\Theta}}{\Theta} D^{\mathrm{int}}(\tilde{\boldsymbol{C}}_{\mathrm{v}}^{\mathrm{F}_i})\mathrm{d}V \\ &+ \sum_{i=1}^{n_{\mathrm{F}}} \frac{1}{2}\int_{\mathcal{B}_0} \dot{\tilde{\boldsymbol{C}}}_{\mathrm{v}}^{\mathrm{F}_i} : \mathbb{V}(\tilde{\boldsymbol{C}}_{\mathrm{v}}^{\mathrm{F}_i}) : \dot{\tilde{\boldsymbol{C}}}_{\mathrm{v}}^{\mathrm{F}_i}\mathrm{d}V + \int_{\mathcal{B}_0} \overline{\boldsymbol{B}} : \dot{\tilde{\boldsymbol{H}}}\mathrm{d}V + \int_{\mathcal{B}_0} \overline{p}\dot{\tilde{J}}\mathrm{d}V + \frac{1}{2}\int_{\mathcal{B}_0} \overline{\tilde{\boldsymbol{S}}}_A : \dot{\tilde{\boldsymbol{C}}}_A\mathrm{d}V + \int_{\mathcal{B}_0} \overline{\boldsymbol{B}}_A : \dot{\tilde{\boldsymbol{H}}}\mathrm{d}V \\ &+ \int_{\mathcal{B}_0} \overline{p}_A\dot{\tilde{J}}\mathrm{d}V + \int_{\mathcal{B}_0} \overline{\boldsymbol{B}}_G \odot_3 \dot{\tilde{\boldsymbol{\Gamma}}}\mathrm{d}V \end{aligned} \tag{11}$$

Here the operator $\odot_3$ represents the triple contraction of two tensors. As in Reference [1] the Piola heat flux vector $\boldsymbol{Q}$ is derived from Duhamel's law. k_{M} and k_{F_i} denotes the material conductivity coefficients for matrix and fiber roving respectively.

$$\boldsymbol{Q} = -\left[\sum_{i=1}^{n_{\mathrm{F}}} J(\tilde{\boldsymbol{C}}_A)\frac{k_{\mathrm{F}_i} - k_{\mathrm{M}}}{\tilde{\boldsymbol{C}}_A : \boldsymbol{M}^i}\boldsymbol{M}^i + kJ(\tilde{\boldsymbol{C}})\tilde{\boldsymbol{C}}^{-1}\right]\nabla\Theta \tag{12}$$

The time evolution of a prescribed boundary displacement is given by $\dot{\boldsymbol{q}}^{\mathrm{ref}}$ with its associated Lagrange multiplier $\boldsymbol{\lambda}_q$. Also the prescribed boundary temperature is given by $\dot{\Theta}^{\mathrm{ref}}$ with its associated Lagrange multiplier $\boldsymbol{\lambda}_\Theta$. The vector $\boldsymbol{g}$ denotes the gravitational force and the vector $\boldsymbol{t}$ the traction load. In order to obtain an energy–momentum scheme, the superimposed pressure $\overline{p}$ and $\overline{p}_A$ as well as the superimposed stress tensor $\overline{\tilde{\boldsymbol{S}}}$ and $\overline{\tilde{\boldsymbol{S}}_A}$ are introduced. Also the superimposed fields $\overline{\boldsymbol{B}}$, $\overline{\boldsymbol{B}}_A$, $\overline{\boldsymbol{B}}_G$ and $\overline{p}_A$ are introduced. The non-negative internal viscous dissipation D^{int} for the matrix as well as the fiber parts is given by

$$D^{\mathrm{int}}(\boldsymbol{\chi}) = \dot{\boldsymbol{\chi}} : \mathbb{V}(\boldsymbol{\chi}) : \dot{\boldsymbol{\chi}} \qquad \mathbb{V}(\boldsymbol{\chi}) = \frac{1}{4}\left(V_{\mathrm{vol}} - \frac{V_{\mathrm{dev}}}{n_{\mathrm{dim}}}\right)\boldsymbol{\chi}^{-1} \otimes \boldsymbol{\chi}^{-1} + \frac{V_{\mathrm{dev}}}{4}\mathbb{I}_{\mathrm{s}} : \boldsymbol{\chi}^{-1} \otimes \boldsymbol{\chi}^{-1}, \tag{13}$$

with respect to $\boldsymbol{\chi}$ as strain-like internal variable tensor With volumetric and deviatoric viscosity constants V_{vol} and V_{dev} respectively. Here $\mathbb{I}_{\mathrm{s}}$ represents the fourth-order symmetric projection tensor and the operator $\otimes$ represents the usual standard dyadic product. The superimposed fields as in Reference [1, 7], are given for example by

$$\overline{\boldsymbol{S}} = \frac{\tilde{\Psi}(1) - \tilde{\Psi}(0) - \int \frac{\partial \Psi_{\mathrm{M}}^{\mathrm{iso}}}{\partial \tilde{\boldsymbol{C}}} : \dot{\tilde{\boldsymbol{C}}} - \int \frac{\partial (\Psi_{\mathrm{M}}^{\mathrm{cap}} + \sum_{i=1}^{n_{\mathrm{F}}} \Psi_{\mathrm{F}_i}^{\mathrm{cap}})}{\partial \Theta} \dot{\Theta} - \int \frac{\partial \Psi_{\mathrm{M}}^{\mathrm{vis}}}{\partial \tilde{\boldsymbol{C}}_{\mathrm{v}}^{\mathrm{M}}} : \dot{\tilde{\boldsymbol{C}}}_{\mathrm{v}}^{\mathrm{M}}}{\dot{\tilde{\boldsymbol{C}}} : \dot{\tilde{\boldsymbol{C}}}} \dot{\tilde{\boldsymbol{C}}} \tag{14}$$

$$\overline{p} = \frac{\tilde{\Psi}(1) - \tilde{\Psi}(0) - \int \frac{\partial (\Psi_{\mathrm{M}}^{\mathrm{iso}} + \Psi_{\mathrm{M}}^{\mathrm{vol}})}{\partial \tilde{J}} \dot{\tilde{J}} - \int \frac{\partial \Psi_{\mathrm{M}}^{\mathrm{coup}}}{\partial \Theta} \dot{\Theta}}{\dot{\tilde{J}} \dot{\tilde{J}}} \dot{\tilde{J}} \tag{15}$$

$$\overline{\boldsymbol{S}}_A = \frac{\tilde{\Psi}(1) - \tilde{\Psi}(0) - \int \frac{\partial \sum_{i=1}^{n_{\mathrm{F}}} \Psi_{\mathrm{F}_i}^{\mathrm{ela}}}{\partial \tilde{\boldsymbol{C}}_A} : \dot{\tilde{\boldsymbol{C}}}_A - \int \frac{\partial \sum_{i=1}^{n_{\mathrm{F}}} \Psi_{\mathrm{F}_i}^{\mathrm{coup}}}{\partial \Theta} \dot{\Theta} - \sum_{i=1}^{n_{\mathrm{F}}} \int \frac{\partial \Psi_{\mathrm{F}_i}^{\mathrm{vis}}}{\partial \tilde{\boldsymbol{C}}_{\mathrm{v}}^{\mathrm{F}_i}} : \dot{\tilde{\boldsymbol{C}}}_{\mathrm{v}}^{\mathrm{F}_i}}{\dot{\tilde{\boldsymbol{C}}}_A : \dot{\tilde{\boldsymbol{C}}}_A} \dot{\tilde{\boldsymbol{C}}}_A \tag{16}$$

and the superimposed fields regarding to the higher-order gradient formulations read as follows

$$\overline{\boldsymbol{B}}_G = \frac{\tilde{\Psi}(1) - \tilde{\Psi}(0) - \int \frac{\partial \Psi_{\mathrm{HOG}}^{\mathrm{C}}}{\partial \tilde{\boldsymbol{\Gamma}}} \odot_3 \dot{\tilde{\boldsymbol{\Gamma}}}}{\dot{\tilde{\boldsymbol{\Gamma}}} \odot_3 \dot{\tilde{\boldsymbol{\Gamma}}}} \dot{\tilde{\boldsymbol{\Gamma}}} \tag{17}$$

From the above energy equations the total energy balance of the system then leads to the following,

$$\dot{\mathcal{H}} = \dot{T} + \dot{\Pi}^{\mathrm{ext}} + \dot{\Pi}^{\mathrm{int}} \tag{18}$$

It is important to note here that the superimposed fields ($\overline{\boldsymbol{S}}$,$\overline{\boldsymbol{B}}$,$\overline{p}$,$\overline{\boldsymbol{S}}_A$,$\overline{\boldsymbol{B}}_A$,$\overline{p}_A$,$\overline{\boldsymbol{B}}_G$), the viscous dissipation D^{int} as well as the Piola heat flux vector $\boldsymbol{Q}$ are defined as parameters and not as arguments. The variation with respect to the variables in the argument of Eq. (18) is performed to obtain total weak forms. With $\int_T \delta_* \dot{\mathcal{H}} \mathrm{d}t \equiv \int_T [\delta_* \dot{T} + \delta_* \dot{\Pi}^{\mathrm{ext}} + \delta_* \dot{\Pi}^{\mathrm{int}}] \mathrm{d}t = 0$ and $\mathbb{P} = \frac{\partial \mathrm{cof}[\tilde{\boldsymbol{C}}]}{\partial \tilde{\boldsymbol{C}}}$ the weak forms are

$$\int_T \int_{\mathcal{B}_0} \left[\frac{1}{\rho_0} \boldsymbol{p} - \dot{\boldsymbol{q}} \right] \cdot \delta_* \dot{\boldsymbol{v}} \mathrm{d}V \mathrm{d}t = 0 \quad \int_T \int_{\mathcal{B}_0} \left[\boldsymbol{P} : \frac{\partial \dot{\boldsymbol{F}}}{\partial \boldsymbol{q}} - \dot{\boldsymbol{p}} \right] \cdot \delta_* \dot{\boldsymbol{q}} \mathrm{d}V \mathrm{d}t = 0 \quad \int_T \int_{\partial \mathcal{B}_0} [-\boldsymbol{\lambda}_q] \cdot \delta_* \dot{\boldsymbol{q}} \mathrm{d}A \mathrm{d}t = 0$$

$$\int_T \int_{\mathcal{B}_0} \left[\eta + \frac{\partial \Psi}{\partial \Theta} \right] \delta_* \dot{\Theta} \mathrm{d}V \mathrm{d}t = 0 \quad \int_T \int_{\mathcal{B}_0} \left[\frac{\mathrm{Div}[\boldsymbol{Q}]}{\Theta} + \frac{D^{\mathrm{int}}(\tilde{\boldsymbol{C}}_{\mathrm{v}}^{\mathrm{M}}) + \sum_{i=1}^{n_{\mathrm{F}}} D^{\mathrm{int}}(\tilde{\boldsymbol{C}}_{\mathrm{v}}^{\mathrm{F}_i})}{\Theta} + \dot{\eta} \right] \delta_* \tilde{\Theta} \mathrm{d}V \mathrm{d}t = 0$$

$$\int_T \int_{\mathcal{B}_0} \frac{1}{2} \left[\dot{\tilde{\boldsymbol{C}}} - 2 \mathbb{I}_{\mathrm{s}} (\tilde{\boldsymbol{F}})^T \dot{\tilde{\boldsymbol{F}}} \right] : \delta_* \tilde{\boldsymbol{S}} \mathrm{d}V \mathrm{d}t = 0 \quad \int_T \int_{\mathcal{B}_0} \left[\tilde{\boldsymbol{P}} - \tilde{\boldsymbol{F}} \tilde{\boldsymbol{S}} \right] : \delta_* \dot{\tilde{\boldsymbol{F}}} \mathrm{d}V \mathrm{d}t = 0$$

$$\int_T \int_{\mathcal{B}_0} \left[\Theta - \tilde{\Theta} \right] \delta_* \dot{\eta} \mathrm{d}V \mathrm{d}t = 0 \quad \int_T \int_{\partial \mathcal{B}_0} \left[\dot{\boldsymbol{q}} - \dot{\boldsymbol{q}}^{\mathrm{ref}}(t) \right] \cdot \delta_* \boldsymbol{\lambda}_q \mathrm{d}A \mathrm{d}t = 0 \quad \int_T \int_{\partial \mathcal{B}_0} \left[\dot{\Theta} - \dot{\Theta}^{\mathrm{ref}}(t) \right] \cdot \delta_* \boldsymbol{\lambda}_q \mathrm{d}A \mathrm{d}t = 0$$

$$\int_T \int_{\mathcal{B}_0} \left[\frac{1}{2} \tilde{\boldsymbol{S}} - \left(\tilde{\boldsymbol{B}} : \mathbb{P} + \frac{p}{2J(\tilde{\boldsymbol{C}})} \mathrm{cof}[\tilde{\boldsymbol{C}}] + \frac{1}{2} \boldsymbol{S}_A + \tilde{\boldsymbol{B}}_A : \mathbb{P} + \frac{p_A}{2J(\tilde{\boldsymbol{C}})} \mathrm{cof}[\tilde{\boldsymbol{C}}] + \boldsymbol{B}_G \odot_3 \frac{\partial \nabla \dot{\tilde{\boldsymbol{C}}}}{\partial \dot{\tilde{\boldsymbol{C}}}} + \overline{\boldsymbol{S}} \right) \right] : \delta_* \dot{\tilde{\boldsymbol{C}}} \mathrm{d}V \mathrm{d}t = 0$$

$$\int_T \int_{\mathcal{B}_0} \left[\frac{\partial \Psi}{\partial \tilde{\boldsymbol{C}}_{\mathrm{v}}^{\mathrm{M}}} + \dot{\tilde{\boldsymbol{C}}}_{\mathrm{v}}^{\mathrm{M}} : \mathbb{V}(\tilde{\boldsymbol{C}}_{\mathrm{v}}^{\mathrm{M}}) \right] : \delta_* \dot{\tilde{\boldsymbol{C}}}_{\mathrm{v}}^{\mathrm{M}} \mathrm{d}V \mathrm{d}t = 0$$

$$\int_T \int_{\mathcal{B}_0} \left[\frac{\partial \Psi}{\partial \tilde{\boldsymbol{C}}_{\mathrm{v}}^{\mathrm{F}_i}} + \dot{\tilde{\boldsymbol{C}}}_{\mathrm{v}}^{\mathrm{F}_i} : \mathbb{V}(\tilde{\boldsymbol{C}}_{\mathrm{v}}^{\mathrm{F}_i}) \right] : \delta_* \dot{\tilde{\boldsymbol{C}}}_{\mathrm{v}}^{\mathrm{F}_i} \mathrm{d}V \mathrm{d}t = 0 \quad \text{for} \quad i = 1, \ldots, n_F$$

$$\int_T \int_{\mathcal{B}_0} \left[\dot{\tilde{\boldsymbol{H}}} - \dot{\text{cof}}[\boldsymbol{C}]\right] : \delta_* \tilde{\boldsymbol{B}} \mathrm{d}V\mathrm{d}t = 0 \qquad \int_T \int_{\mathcal{B}_0} \left[\tilde{\boldsymbol{B}} - \left[\frac{\partial \Psi}{\partial \tilde{\boldsymbol{H}}} + \overline{\boldsymbol{B}}\right]\right] : \delta_* \dot{\tilde{\boldsymbol{H}}} \mathrm{d}V\mathrm{d}t = 0$$

$$\int_T \int_{\mathcal{B}_0} \left[\dot{\tilde{J}} - \dot{J}\right] \delta_* p \mathrm{d}V\mathrm{d}t = 0 \qquad \int_T \int_{\mathcal{B}_0} \left[p - \left[\frac{\partial \Psi}{\partial \tilde{J}} + \overline{p}\right]\right] \delta_* \dot{\tilde{J}} \mathrm{d}V\mathrm{d}t = 0$$

$$\int_T \int_{\mathcal{B}_0} \frac{1}{2}\left[\dot{\tilde{\boldsymbol{C}}}_A - \dot{\tilde{\boldsymbol{C}}}\right] : \delta_* \boldsymbol{S}_A \mathrm{d}V\mathrm{d}t = 0 \qquad \int_T \int_{\mathcal{B}_0} \left[\frac{1}{2}\boldsymbol{S}_A - \left[\frac{\partial \Psi}{\partial \tilde{\boldsymbol{C}}_A} + \overline{\boldsymbol{S}}_A\right]\right] : \delta_* \dot{\tilde{\boldsymbol{C}}}_A \mathrm{d}V\mathrm{d}t = 0$$

$$\int_T \int_{\mathcal{B}_0} \left[\dot{\boldsymbol{H}}_A - \dot{\text{cof}}[\boldsymbol{C}]\right] : \delta_* \tilde{\boldsymbol{B}}_A \mathrm{d}V\mathrm{d}t = 0 \qquad \int_T \int_{\mathcal{B}_0} \left[\tilde{\boldsymbol{B}}_A - \left[\frac{\partial \Psi}{\partial \tilde{\boldsymbol{H}}_A} + \overline{\boldsymbol{B}}_A\right]\right] : \delta_* \dot{\tilde{\boldsymbol{H}}}_A \mathrm{d}V\mathrm{d}t = 0$$

$$\int_T \int_{\mathcal{B}_0} \left[\dot{\tilde{J}}_A - \dot{J}\right] \delta_* p_A \mathrm{d}V\mathrm{d}t = 0 = 0 \qquad \int_T \int_{\mathcal{B}_0} \left[p_A - \left[\frac{\partial \Psi}{\partial \tilde{J}_A} + \tilde{p}_A\right]\right] \delta_* \dot{\tilde{J}}_A \mathrm{d}V\mathrm{d}t = 0$$

$$\int_T \int_{\mathcal{B}_0} \left[\nabla(\dot{\tilde{\boldsymbol{C}}}) - \dot{\tilde{\boldsymbol{\Gamma}}}\right] \odot_3 \delta_* \boldsymbol{B}_G \mathrm{d}V\mathrm{d}t = 0 \qquad \int_T \int_{\mathcal{B}_0} \left[\boldsymbol{B}_G - \left[\frac{\partial \Psi}{\partial \tilde{\Gamma}} + \overline{\boldsymbol{B}}_G\right]\right] \odot_3 \delta_* \dot{\tilde{\boldsymbol{\Gamma}}} \mathrm{d}V\mathrm{d}t = 0$$

In the next step, we discretize all quantities over the elements in space and time and transform the integrals to reference elements. We use Lagrangian shape functions N for space approximation as in Reference [10]) and different mixed fields are approximated independently. For Lagrangian multipliers similar shape functions are used as their corresponding mixed fields. Similarly we use Lagrangian shape functions in time as well as in Reference [1], which are given by

$$M_i(\alpha) = \prod_{\substack{j=1 \\ j\neq i}}^{k+1} \frac{\alpha - \alpha_j}{\alpha_i - \alpha_j},\ 1 \leq i \leq k+1 \qquad \tilde{M}_i(\alpha) = \prod_{\substack{j=1 \\ j\neq i}}^{k} \frac{\alpha - \alpha_j}{\alpha_i - \alpha_j}, 1 \leq i \leq k \tag{19}$$

where k is the polynomial degree in time. The time rate variables and mixed fields are approximate by $k+1$-th order Lagrange polynomials at each time step

$$(\bullet)^{e,h} = \sum_{I=1}^{k+1} \sum_{A=1}^{n_{no}} M_I(\alpha) \mathrm{N}^A(\boldsymbol{\xi}) (\bullet)_I^{eA} \quad \text{with} \quad \alpha(t) = \frac{t - t_n}{t_{n+1} - t_1} \tag{20}$$

where n_{no} is the number of nodes of the spatial discretization. Similarly, the approximation of Lagrangian multipliers and variation fields takes the form

$$(\bullet)^{e,h} = \sum_{I=1}^{k} \sum_{A=1}^{n_{no}} \tilde{M}_I \mathrm{N}^A (\bullet)_I^{eA} \tag{21}$$

We approximate each integral with the corresponding Gaussian quadrature rule. After eliminating $\boldsymbol{p}$ and η, the resulting tangent matrices are condensed out to a displacement and temperature formulation at the element level as described in Reference [2]. Note, all mixed fields, except $\boldsymbol{q}$ and Θ, are discontinuous at the boundaries of spatial elements. The internal variables $\tilde{\boldsymbol{C}}_{\mathrm{v}}^{\mathrm{M}}$ and $\tilde{\boldsymbol{C}}_{\mathrm{v}}^{\mathrm{F}_i}$ are solved on the element level using the Newton-Raphson method, not at each spatial quadrature point. Since the higher-order gradient formulation results in internal torques, the conservation of angular momentum must be corrected. For this, following the procedure from Reference [14], we obtain a time-integerator that conserves total

angular momentum for formulation based on $\boldsymbol{C}$

$$\mathcal{J}_{n+1} - \mathcal{J}_n = \int_{t_n}^{t_n+1} \int_{\mathcal{B}_0} \left[\boldsymbol{B}_G \odot_3 \frac{\partial \nabla \dot{\tilde{\boldsymbol{C}}}}{\partial \dot{\tilde{\boldsymbol{C}}}} \times \tilde{\boldsymbol{F}} \right] \mathrm{d}V \mathrm{d}t + \int_{t_n}^{t_n+1} \int_{\partial \mathcal{B}_0} [\boldsymbol{q} \times \boldsymbol{\lambda}_q] \mathrm{d}A \mathrm{d}t + \int_{t_n}^{t_n+1} \int_{\mathcal{B}_0} [\boldsymbol{q} \times \rho_0 \boldsymbol{g}] \mathrm{d}V \mathrm{d}t \tag{22}$$

We use our In-House Matlab code fEMcon based on the implementation and ideas shown in Reference [10]. To solve the linear systems of equations we use the Pardiso solver from Reference [11]. For the assembly procedure of all n_{el} finite elements, we use the fast sparse routine shown in Reference [12].

3 NUMERICAL EXAMPLES

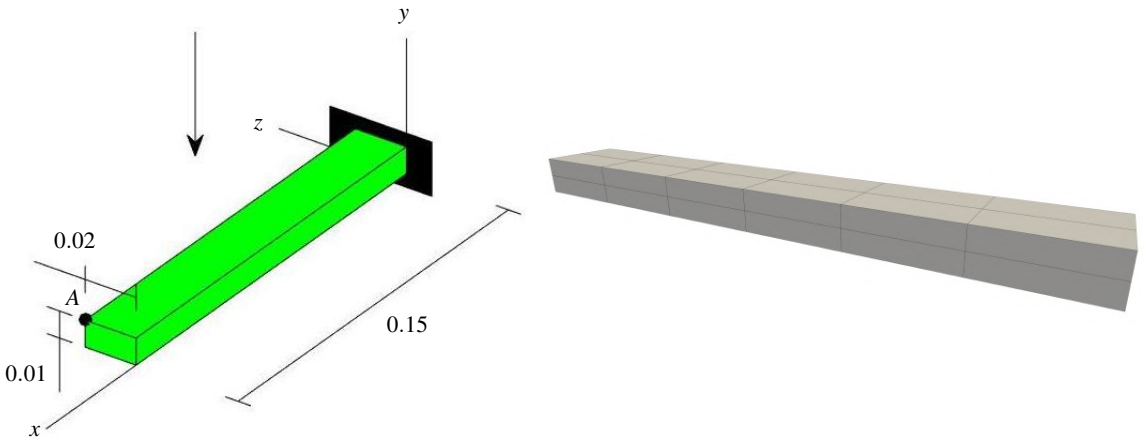

Figure 1: Geometry and configuration of the cantilever beam for $n_{el} = 24$.

As first numerical example serves a simple cantilever beam which oscillates in a gravitational field. The geometry and configuration can be found in Figure 1. The corresponding strain energy functions are

$$\Psi_{\mathrm{M}}^{\mathrm{iso}} = \frac{\varepsilon_1}{2}(\mathrm{tr}[\boldsymbol{C}])^2 + \frac{\varepsilon_2}{2}(\mathrm{tr}[\mathrm{cof}[\boldsymbol{C}]])^2 - \varepsilon_3 \ln(J) \quad \Psi_{\mathrm{M}}^{\mathrm{vol}} = \frac{\varepsilon_4}{2}(J^{\varepsilon_5} + J^{-\varepsilon_5} - 2)$$

$$\Psi_{\mathrm{F_1}}^{\mathrm{ela}} = \varepsilon_6 \left(\frac{1}{\varepsilon_7 + 1}(\mathrm{tr}[\boldsymbol{C}\boldsymbol{M}_1])^{\varepsilon_7+1} + \frac{1}{\varepsilon_8 + 1}(\mathrm{tr}[\mathrm{cof}[\boldsymbol{C}]\boldsymbol{M}_1])^{\varepsilon_8+1} + \frac{1}{\varepsilon_9}\det[\boldsymbol{C}]^{-\varepsilon_9} \right) \quad \Psi_{\mathrm{H_1}} = l^2 (I_6)^2$$

$$\Psi_X^{\mathrm{cap}} = c_X^0(1 - \Theta_\infty c_X^1)(\Theta - \Theta_\infty - \Theta \ln \frac{\Theta}{\Theta_\infty}) - \frac{1}{2} c_X^0 c_X^1 (\Theta - \Theta_\infty)^2$$

$$\Psi_{\mathrm{M}}^{\mathrm{vis}} = \Psi_{\mathrm{M}}^{\mathrm{iso}}(\boldsymbol{C}(\tilde{\boldsymbol{C}}_{\mathrm{v}}^{\mathrm{M}})^{-1}) + \Psi_{\mathrm{M}}^{\mathrm{vol}}(\boldsymbol{C}(\tilde{\boldsymbol{C}}_{\mathrm{v}}^{\mathrm{M}})^{-1}) \quad \Psi_{\mathrm{F_1}}^{\mathrm{vis}} = \Psi_{\mathrm{F_1}}^{\mathrm{ela}}(\boldsymbol{C}(\tilde{\boldsymbol{C}}_{\mathrm{v}}^{\mathrm{F_1}})^{-1})$$

The strain energy function of the matrix $\Psi_{\mathrm{M}}^{\mathrm{iso}}$ and the fiber $\Psi_{\mathrm{F_1}}^{\mathrm{ela}}$ can be found in Reference [9] and for the capacitive part the function Ψ_X^{cap} in Reference [1] . We use a quadratic mesh (27 nodes) with $n_{el} = 24$ and approximate $\tilde{J}$ constant and $\tilde{\boldsymbol{C}}_A$ constant as well to avoid potential locking effect. We introduce a length scale parameter l^2 with $c = \varepsilon_1 l^2$ for the material parameters of $\Psi_{\mathrm{H_1}}$. We set the material parameters in such a way that we have high incompressibility ($\nu = 0.4995$) and very stiff fibers ($\varepsilon_6 = 10 \cdot 10^6$,$c = 1$). We also set a high viscosity, for matrix as for the fiber. The heat conduction and the thermo-mechanical

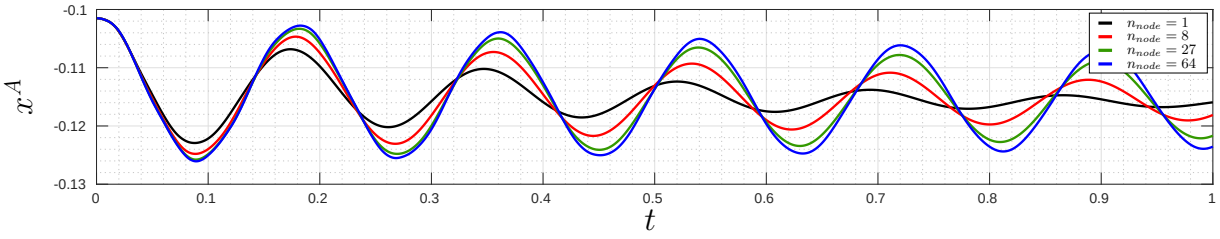

Figure 2: Trajectorie of point A for different local spatial approximations of the viscous mixed field.

Table 1: Compurational time for diffrent spatial approximation of $\tilde{\boldsymbol{C}}_{\mathrm{v}}^{\mathrm{M}}$ and $\tilde{\boldsymbol{C}}_{\mathrm{v}}^{\mathrm{F}_i}$.

	$n_{node} = 1$	$n_{node} = 8$	$n_{node} = 27$	$n_{node} = 64$
t_{Res}	$0.54s$	$1.55s$	$3.80s$	$17.06s$
t_{Tang}	$0.93s$	$4.63s$	$12.33s$	$47.20s$
t_{Solver}	$3.31s$	$3.21s$	$3.42s$	$3.33s$
t_{CPU}	$4.78s$	$9.39s$	$19.55s$	$67,88s$

coupling are set to low values ($k < 1$). We investigate here the influence of the local spatial approximation of the viscous mixed field. Therefor we compare four different elments. An constant ($n_{node} = 1$), an linear ($n_{node} = 8$), an quadtratic ($n_{node} = 27$) and an cubic ($n_{node} = 64$) hexahedral element. In Figure 2 we can see that there are smaller differences for the linear, quadratic and cubic element for the trajectorie of point A. Furthermore, one can observe the typical decrease of the amplitude for a viscous oscillation. If we now look at the computation times in Table 1, we can see the strong savings due to the lower polynomial degree for $\tilde{\boldsymbol{C}}_{\mathrm{v}}^{\mathrm{M}}$ and $\tilde{\boldsymbol{C}}_{\mathrm{v}}^{\mathrm{F}_i}$. This is only possible because we formulate $\tilde{\boldsymbol{C}}_{\mathrm{v}}^{\mathrm{M}}$ and $\tilde{\boldsymbol{C}}_{\mathrm{v}}^{\mathrm{F}_i}$ as an independent mixed field.

Our second example is the turbine from Reference [15]. The geometry and configuration can be found

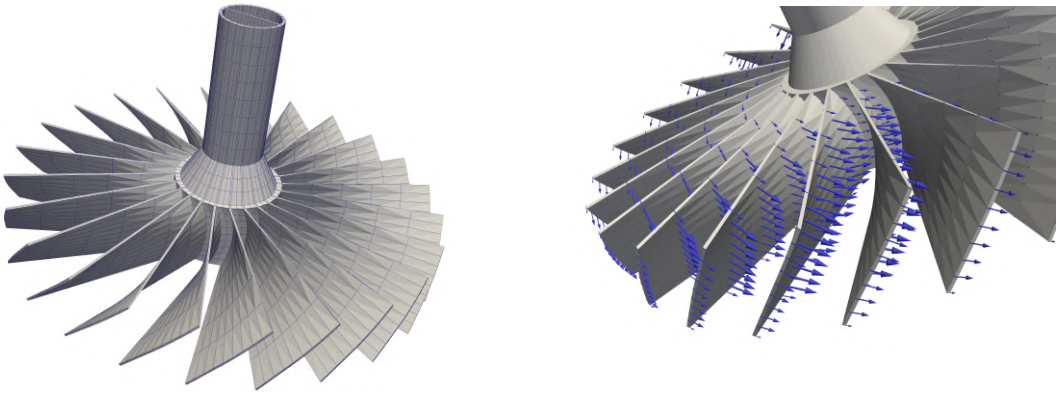

Figure 3: Geometry, discretization and Neumann boundary for the turbine.

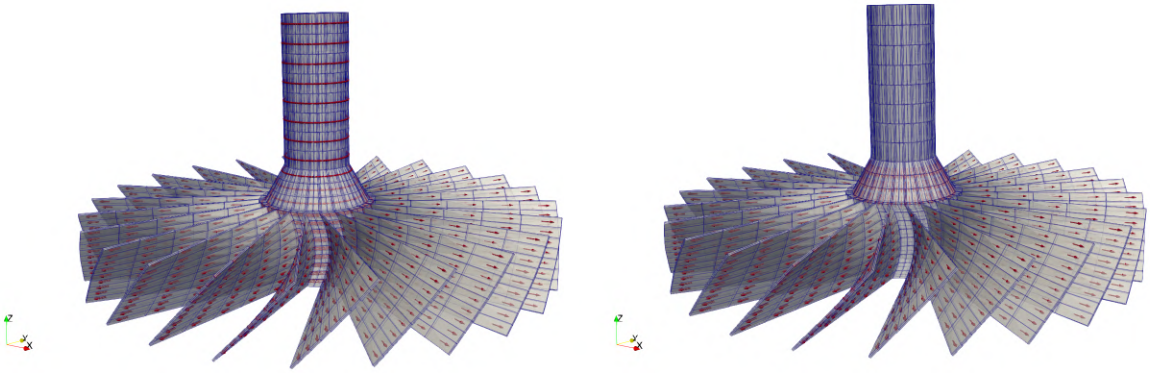

Figure 4: Fiber directions of the turbine. Left - Circumferential fiber with high mechanical stiffness Right - Vertical fiberswith high thermal conductivity.

in Figure 3. The corresponding strain energy functions are

$$\Psi_{\mathrm{M}}^{\mathrm{iso}} = \frac{\varepsilon_1}{2}(\mathrm{tr}[\boldsymbol{C}] - 3 - 2\ln(J)) \quad \Psi_{\mathrm{M}}^{\mathrm{vol}} = \frac{\varepsilon_2}{2}\left(\ln(J)^2 + (J-1)^2\right)$$
$$\Psi_{X}^{\mathrm{cap}} = c_X^0(1-\Theta_\infty c_X^1)(\Theta - \Theta_\infty - \Theta\ln\frac{\Theta}{\Theta_\infty}) - \frac{1}{2}c_X^0 c_X^1(\Theta-\Theta_\infty)^2$$
$$\Psi_{\mathrm{F}_X}^{\mathrm{ela}} = \frac{\varepsilon_3}{2}(\mathrm{tr}[\boldsymbol{C}\boldsymbol{M}_X] - 1)^2 \quad \Psi_{\mathrm{H}_X} = l^2\,(I_6)^2$$
$$\Psi_{\mathrm{M}}^{\mathrm{vis}} = \Psi_{\mathrm{M}}^{\mathrm{iso}}(\boldsymbol{C}(\tilde{\boldsymbol{C}}_{\mathrm{v}}^{\mathrm{M}})^{-1}) + \Psi_{\mathrm{M}}^{\mathrm{vol}}(\boldsymbol{C}(\tilde{\boldsymbol{C}}_{\mathrm{v}}^{\mathrm{M}})^{-1}) \quad \Psi_{\mathrm{F}_1}^{\mathrm{vis}} = \Psi_{\mathrm{F}_X}^{\mathrm{ela}}(\boldsymbol{C}(\tilde{\boldsymbol{C}}_{\mathrm{v}}^{\mathrm{F}_X})^{-1})$$

The elastic part and the corrosponding material parameters of the fiber roving $\Psi_{\mathrm{F}}^{\mathrm{ela}_X}$ can be found in [13]. Figure 4 shows the fiber configuration. On the one hand, a fiber is placed along the blade and on the other hand, a fiber surrounds the shaft. Furthermore, a second fiber is placed horizontally in the shaft. We use a quadratic mesh (27 nodes) with $n_{el} = 24$ and approximate $\tilde{J}$ linear and $\tilde{\boldsymbol{C}}_A$ constant to avoid potential locking effect. A pressure boundary condition of $p = 200$ is applied to the blades and also a constant temperature as Dirichlet boundary condition is set ($\Theta = 400$). To ensure that the turbine is fixed, a dirichlet boundary condition is set in z-direction. The material parameter for the elastic part are set as shown in Reference [13]. Also the fiber bending stiffenes is set to $c = 10$. The thermo-mechanical coupling is low as well as the viscosity. For the values of the heat conduction we distingush between the two fibers. The first fiber has a low heat conduction ($k = 0.1$) and the horizontally fiber has a high heat conduction ($k = 100$) to conduct the heat directly out of the blase. We have done a simulation with and without the second fiber. In Figure 3 we see the result after $T = 30s$. As can be seen, the additional fiber conducts the heat out of the blade. In case of the fiber bending stiffenes it is important to look at the angular momentum balance to check the correct calculation of the internal moments. In Figure 6 we see the angular momentum is perfectly preserved.

Our last example is an rotor as shown in Figure 8. We use the same material setting as for the turbine, but with only the first fiber. We use a linear hexahedral mesh (8 nodes) with $n_{el} = 32742$ and approximate $\tilde{J}$ linear and $\tilde{\boldsymbol{C}}_A$ constant to avoid potential locking effect. As boundary condition we use this time a given rotation at the inner side of the rotor ($\Omega = 2\pi$) In Figure X we see the v. Mises stress and the temperature

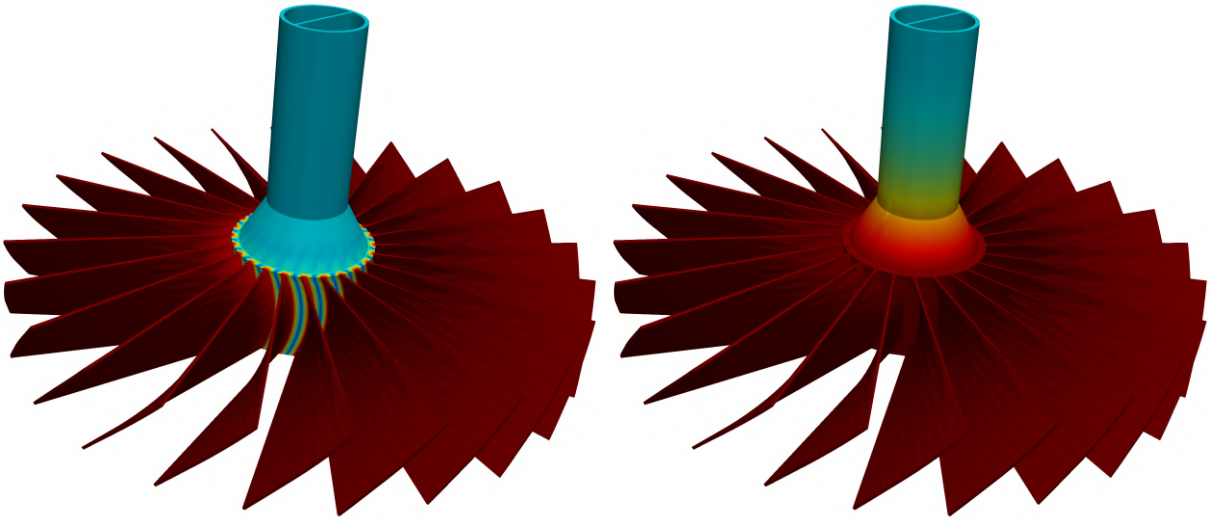

Figure 5: Actual configuration and temperature distribution for one (left) and two (right) fibers.

distribution at $T = 10$. As expected, the highest stress occurs at the end of the blade, since the highest speeds occur here. Here we see also the temperature increases due to dissipation and thermo-mechanical coupling. Finally, we look at the preservation of energy error in Figure 9 and can see that it is perfectly preserved.

4 Conclusion

Excellent performance of the mixed elements is still preserved in a thermo-viscoelastic and higher-order gradient context and also the higher-order time integrators conserves the energy and momentum. Also, all relevant effects, such as heat conduction, directional heat conduction, thermo-mechanical coupling and viscous dissipation, are represented in combination with a higher-order gradient formulation. The independent approximation of the viscous variable also ensures a strong saving in computing time.

Acknowledgments

The authors thank the 'Deutsche Forschungsgemeinschaft (DFG)' for the financial support of this work under the grant GR3297/4-2 and GR3297/6-1 as well as Matthias Bartelt (GR 3297/2-2) for providing the programming basis for the current implementation.

REFERENCES

[1] Groß, M., Dietzsch, J., and Bartelt, M. (2018). Variational-based higher-order accurate energy–momentum schemes for thermo-viscoelastic fiber-reinforced continua. *Comput. Methods Appl. Mech. Engrg.*, 336, 353–418. https://doi.org/10.1016/j.cma.2018.03.019

[2] Schröder, J., Viebahn, V., Wriggers, and P., Balzani, D. (2016). A novel mixed finite element for finite anisotropic elasticity; the SKA-element Simplified Kinematics for Anisotropy. *Comput. Methods Appl. Mech. Engrg.*, 310:475–494.

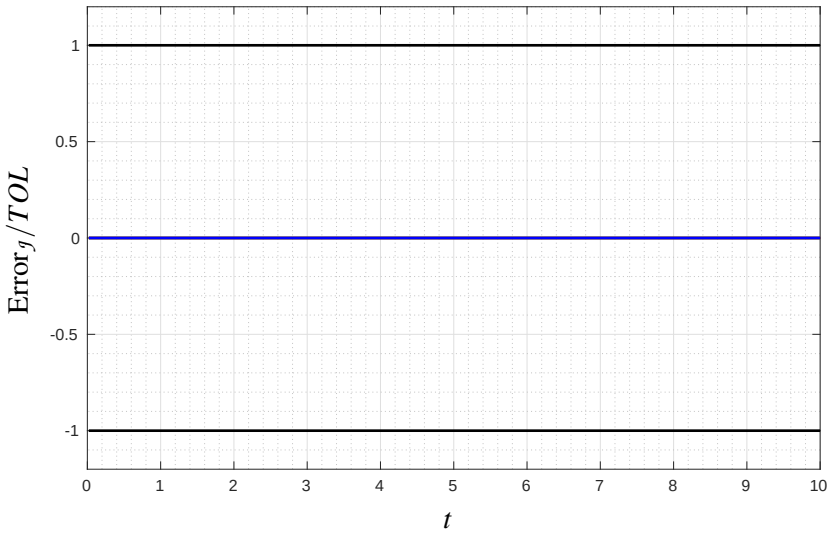

Figure 6: Error of angular momentum $\mathcal{J}$ for the the turbine.

[3] Dietzsch, J. and Groß, M. GALERKIN-BASED TIME INTEGRATION OF FINITE ANISOTROPIC ELASTODYNAMICS. in ECCOMAS Congress 2018 (2018).

[4] Dietzsch J., Groß M. and Kalaimani I. (2021), Energy-momentum time integration of gradient-based models for fiber-bending stiffness in anisotropic thermo-viscoelastic continua, VI ECCOMAS Young Investigators Conference, Valencia, Spain, 07-09 July 2021, abstract p. 120 , paper p. 89, DOI: http://dx.doi.org/10.4995/YIC2021.2021.15320 .

[5] Asmanoglo, T., Menzel., A. (2017) A multi-field finite element approach for the modelling of fibre-reinforced composites with fibre-bending stiffness. *Comput. Methods Appl. Mech. Engrg.*, 317:1037–1067.

[6] Ferretti, M., Madeo, A., dell'Isola, F., & Boisse, P. (2014). Modeling the onset of shear boundary layers in fibrous composite reinforcements by second-gradient theory. Zeitschrift Fur Angewandte Mathematik und Physik, 65(3), 587–612.

[7] J. Dietzsch and M. Groß, Mixed Finite Element Formulations for Polyconvex Anisotropic Material Formulations in WCCM-ECCOMAS2020.

[8] Simo, J. C., Taylor, R. L., and Pister, K. S. (1985). Variational and projection methods for the volume constraint in finite deformation elasto-plasticity. *Comput. Methods Appl. Mech. Engrg.*, 51(1–3), 177–208. https://doi.org/10.1016/0045-7825(85)90033-7

[9] Schröder, J., Wriggers, P., and Balzani, D. (2011). A new mixed finite element based on different approximations of the minors of deformation tensors. *Comput. Methods Appl. Mech. Engrg.*, 49:3583–3600.

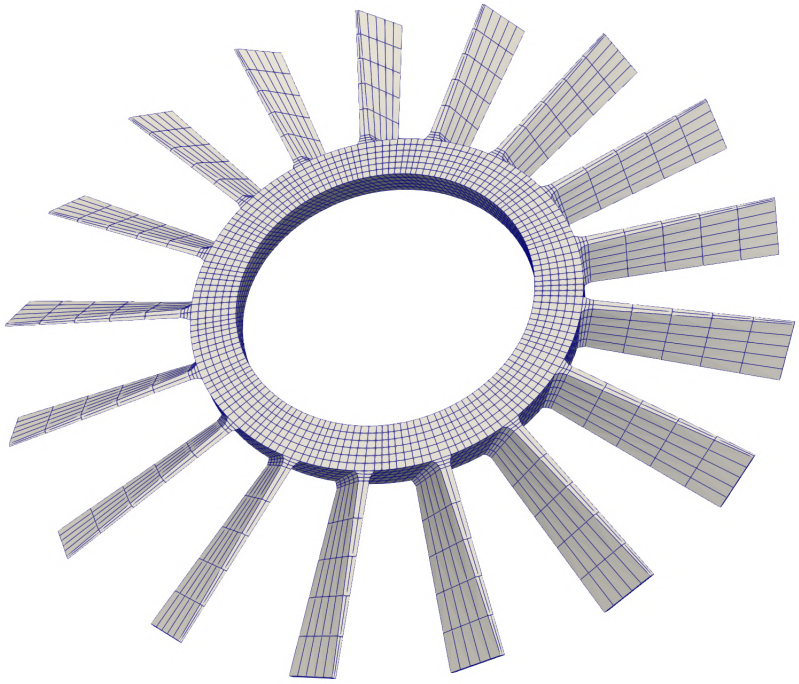

Figure 7: Geometry and discretization of the rotor.

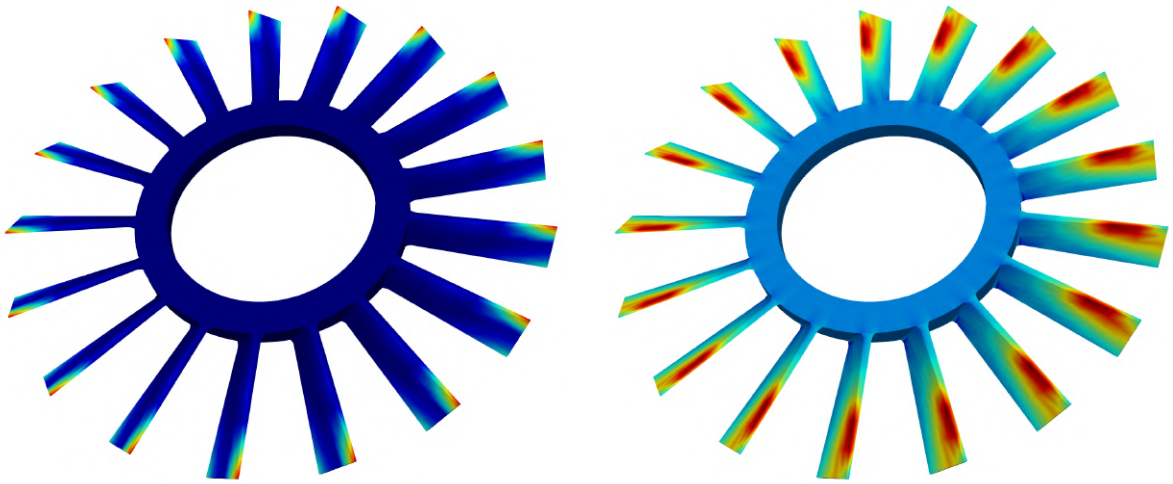

Figure 8: Actual configuration, v Mises stress (left) and temperature distribution (right) of the rotor.

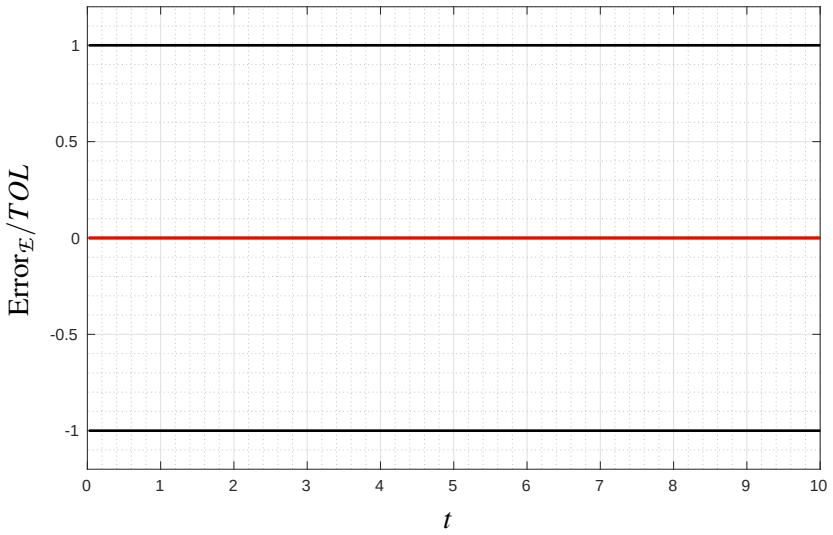

Figure 9: Error of energy $\mathcal{E}$ for the the rotor.

[10] Bartelt, M., Dietzsch, J., and Groß, M. (2018). Efficient implementation of energy conservation for higher order finite elements with variational integrators. *Math. Comput. Simulat.*, 150, 83–121. https://doi.org/10.1016/j.matcom.2018.03.002

[11] Alappat, C., Basermann, A., Bishop, A. R., Fehske, H., Hager, G., Schenk, O., Thies, J., and Wellein, G. (2020). A Recursive Algebraic Coloring Technique for Hardware-efficient Symmetric Sparse Matrix-vector Multiplication. *ACM Transactions on Parallel Computing*, 7(3). https://doi.org/10.1145/3399732

[12] Engblom, S., and Lukarski, D. (2016). Fast Matlab compatible sparse assembly on multicore computers. *Parallel Computing*, 56, 1–17. https://doi.org/10.1016/j.parco.2016.04.001

[13] Dal, H., Gültekin, O., Aksu Denli, F., and Holzapfel, G. A. (2017). Phase-Field Models for the Failure of Anisotropic Continua. *PAMM*, 17(1). https://doi.org/10.1002/pamm.201710027

[14] Groß, M., Dietzsch, J., and Röbiger, C. (2020). Non-isothermal energy–momentum time integrations with drilling degrees of freedom of composites with viscoelastic fiber bundles and curvature–twist stiffness. Computer Methods in Applied Mechanics and Engineering, 365, 112973. https://doi.org/10.1016/j.cma.2020.112973

[15] Noels, L., Stainier, L. and Ponthot, J.-P., A Consistent Dissipative Time Integration Scheme for Structural Dynamics: Application to Rotordynamics. *45th AIAA/ASME/ASCE/AHS/ASC Structures, Structural Dynamics & Materials Conference*, pp. 1945, (2004).